Science of the Total Environment 955 (2024) 177025

Contents lists available at ScienceDirect

Science of the Total Environment

journal homepage: www.elsevier.com/locate/scitotenv

Mapping intertidal microphytobenthic biomass with very high-resolution remote sensing imagery in an estuarine system

Alejandro Román [a,*], Simon Oiry [b], Bede F.R. Davies [b], Philippe Rosa [b], Pierre Gernez [b], Antonio Tovar-Sánchez [a], Gabriel Navarro [a], Vona Méléder [b], Laurent Barillé [b]

[a] Institute of Marine Sciences of Andalusia (ICMAN), Spanish National Research Council (CSIC), Department of Ecology and Coastal Management, Puerto Real 11519, Spain

[b] Nantes Université, Institut des Substances et Organismes de la Mer, ISOMer, UR 2160, F-44000 Nantes, France

HIGHLIGHTS

- Very high-resolution UAV data was used to establish MPB biomass spatial patterns.
- Flight altitudes were varied to properly align multispectral pixels with cored surfaces.
- A 0.3 mm/px spatial resolution was achieved by holding the multispectral sensor at 1 m altitude.
- A robust correlation was found in the model between spectral indices and *in-situ* chlorophylls.

GRAPHICAL ABSTRACT

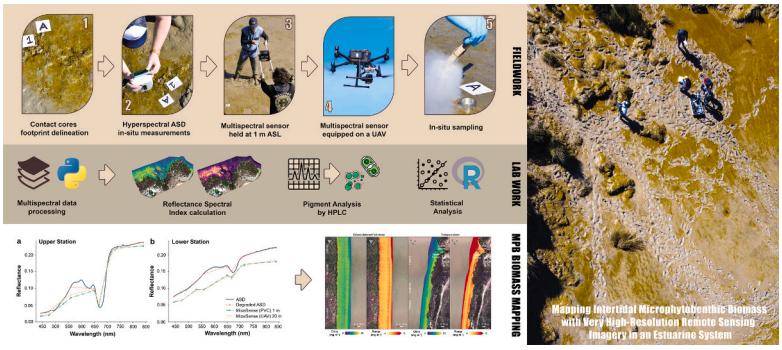

ARTICLE INFO

Editor: Ouyang Wei

Keywords:
Benthic microalgae
Unmanned aerial vehicle (UAV)
Spectral index
Biomass
Multispectral

ABSTRACT

Microphytobenthos (MPB) contributes significantly to estuarine primary production, so that quantifying its biomass is crucial for assessing their ecosystem functioning. Conventional sampling methods are labour-intensive, logistically challenging, and cannot provide a comprehensive spatial distribution map of MPB biomass. Satellite imagery has offered a feasible alternative for mapping large areas at various temporal and spatial resolutions. However, no imaging device with a spatial resolution consistent with the few square centimetres sampled *in-situ* has been used in the field. This makes it challenging to accurately relate field biomass measurements with remotely sensed radiometric observations. In this study, two similar multispectral sensors were mounted on an unmanned aerial vehicle (UAV) at different altitudes, as well as on a custom-built device specifically designed to acquire images at ~1 m altitude, in order to collect very-high spatial resolution reflectance data of MPB biofilms at the Guadalquivir Estuary (Spain) mudflats. In addition, a hyperspectral spectroradiometer acquiring *in-situ* field reflectance was used for validation. Simultaneously, MPB samples were collected using a 2 mm depth contact corer method, which were analysed through high-performance liquid chromatography (HPLC) to measure the concentrations of major MPB pigments. To assess the relationship between the MPB pigments and different reflectance-based spectral indices, generalised linear mixed effects models (GLMMs) were used, achieving a significant positive relationship between chlorophylls and all spectral indices tested. These models were used to map microphytobenthic biomass, yielding a mean biomass in the range of

* Corresponding author.

https://doi.org/10.1016/j.scitotenv.2024.177025
Received 21 May 2024; Received in revised form 15 October 2024; Accepted 15 October 2024
Available online 19 October 2024

30–50 mg Chl-a m^{-2} in the Guadalquivir estuary during late winter. This study demonstrates the potential of low-altitude/high spatial resolution radiometric imaging as an efficient, rapid, and non-destructive addition to *in-situ* measurements of MPB biomass, providing exciting perspectives for the monitoring of estuarine systems on a millimetric scale of variability.

1. Introduction

Estuarine intertidal areas are hotspots of primary production and nutrient cycling (Daggers et al., 2018; Frakenbach et al., 2020), responsible for up to 20 % of the ocean gross primary production (~ 500 Mt. of carbon), although they represent <0.03 % of surface marine environments (Cahoon, 1999; Park et al., 2024; Pinckney, 2018). Microphytobenthos (MPB, unicellular photosynthetic eukaryotes and cyanobacteria), colonise the sediment's superficial layer forming biofilms in the intertidal and shallow subtidal areas (MacIntyre et al., 1996; Underwood and Kromkamp, 1999). This biofilm can contribute significantly to estuarine primary production (Frakenbach et al., 2020; Spilmont et al., 2006; Underwood and Kromkamp, 1999) and provides a wide variety of ecosystem services (Hope et al., 2019; Park et al., 2024), such as a significant food source for benthic macrofauna (Blanchard et al., 2001; Daggers et al., 2020a; Middelburg et al., 2000), mediating nutrient and oxygen exchange in the sediment-water interface, moderating carbon flows in coastal sediments by acting as a natural CO_2 sink (Guarini et al., 2000; Jiménez-Arias et al., 2020; Otani and Endo, 2018), and reducing erosive processes by stabilising sediment surface (Miller et al., 1996; Stal, 2010). As a result, MPB holds significant potential as a biological quality indicator, and quantifying its biomass is crucial for estimating the health of estuarine systems (Trobajo and Sullivan, 2010).

MPB communities exhibit a high spatio-temporal heterogeneity partly shaped by tidal exposure and sediment grain size (Benyoucef et al., 2014; Jacobs et al., 2021; Kwon et al., 2020; Ribeiro et al., 2021). As a consequence, MPB biofilms exposed to daylight for longer periods and characterised by finer-grain sediments (*i.e.* silt and mud) exhibit higher MPB biomass due to extended photosynthetic periods, unless they are affected by high levels of irradiance and temperatures, which can inhibit their growth due to photoinhibition, photodegradation, or desiccation (Jacobs et al., 2021; Savelli et al., 2021; Underwood et al., 1998; Van der Wal et al., 2010). MPB biomass is commonly estimated from the content of photosynthetic pigments, more commonly the Chl-a content (*e.g.* MacIntyre et al., 1996). This content could be determined directly from samples of a thin layer of the upper sediment's surface through the analysis of photosynthetic pigments by high-performance liquid chromatography (HPLC) (*e.g.* Barillé et al., 2011; Brotas and Plante-Cuny, 2003; Reddin et al., 2022), or indirectly using UV-VIS spectroscopy (*e.g.* Daggers et al., 2018; Douglas et al., 2023). However, it is challenging to collect samples on intertidal flats which are often hard to access due to muddy sediment. Indeed, traditional sampling methods with coring devices, and in particular the requirement to flash-froze the samples using liquid nitrogen, are labour-intensive, logistically challenging, and cannot be used to obtain an extensive map of MPB biomass spatial distribution (*e.g.* Guarini et al., 1998; Orvain et al., 2012), or to obtain MPB time-series at high temporal resolution and over long periods (*e.g.* Méléder et al., 2005; Zhang et al., 2021).

Remote sensing-based approaches provide a viable alternative for mapping extensive MPB-covered areas with high temporal and spatial resolutions, while also reducing costs, time, and efforts (Haro et al., 2022; Oiry and Barillé, 2021). Many studies have used the normalized difference vegetation index (NDVI) as a proxy of benthic chlorophyll-a concentration, employing a range of multispectral satellite sensors (*e.g.* Benyoucef et al., 2014; Brito et al., 2013; Daggers et al., 2018, 2020b; Echappé et al., 2018) that acquire reflectance measurements in both red and near-infrared spectral bands (Tucker, 1979). More complex indices can be obtained at hyperspectral resolution, making it possible to detect the absorption signature of pigments other than chlorophyll-a, or to apply different methods for processing reflectance spectra, such as derivative analysis (Barillé et al., 2011; Jesus et al., 2014) or indices derived from radiative transfer modelling (Launeau et al., 2018). However, establishing a quantitative and precise relationship between remotely-sensed radiometric measurements and field measurements of MPB biomass remains challenging due to the significant variability between the pixel size of satellite imagery and the few cm^2 extracted by core sampling systems (Brito et al., 2013). In fact, the lack of consistency between field and remote measurements in previous attempts was due to mismatches between the locations of the pixels and sampling stations, spectral mixtures from sub-pixel variability in the upwelling radiance, or depth differences between core sampling and the optical layer imaged by the remote sensor (*e.g.* Barillé et al., 2011; Jesus et al., 2006; Kromkamp et al., 2006; Launeau et al., 2018).

In this work, we show that very high-resolution (VHR) (*i.e.* centimetric or millimetric scale) remote sensing data can be consistently used to establish biomass relationships deriving from natural assemblages. Most importantly, reflectance measurements over VHR pixels can be perfectly aligned with the cored surfaces, enabling accurate matchups and computation of validation metrics that would otherwise be impossible to obtain with the spatial resolution of any satellite sensors. Two similar multispectral sensors were mounted on board an unmanned aerial vehicle (UAV), as well as on a hand-held platform made of two PVC poles specifically designed to maintain the sensor at a distance of ~1 m above the MPB biofilm, to find the exact alignment between field samples and reflectance measurements. Different flight altitudes above sea level (ASL) were tested to determine the optimal approach in terms of ground sampling distance (GSD). Our main objective was to establish a quantitative relationship between measured MPB pigments collected from surface sediment and various spectral indices derived from VHR remote sensing data, to be applied at a varied scale of observations. This study provides a standardised framework for the application of UAV technology in modelling MPB biomass in estuarine ecosystems, showing the potential of this tool for future research aimed at upscaling the technique to satellite remote sensing.

2. Material and methods

2.1. Study location

The Guadalquivir Estuary (Fig. 1A) constitutes one of the most important estuaries in Western Europe, bordering the Doñana Natural and National Parks, which were designated as a UNESCO-MAB Biosphere Reserve in 1980 (UNESCO MAB, n.d.) and a World Heritage site in 1994 (UNESCO WHC, n.d.). Its catchment areas are dominated by agriculture, salt production, and aquaculture activities which, along with the construction of >150 reservoirs since the beginning of the 20th century, have contributed to the disconnection of the estuary from the tidal flats and marshes in its surroundings (Ruiz et al., 2015). In addition, it is the only navigable estuary in Spain, and the channel is periodically dredged, thus contributing to increase water turbidity to high levels in areas accumulating suspended particulate matter (Caballero et al., 2018; Miró et al., 2022). It is a mesotidal estuary, with a tidal range of approximately 3.5 m in spring tides, supporting the appearance of MPB biofilms during low tide (Pérez-Rodríguez et al., 2024). The selected sampling area was located in a mudflat (36°53′40.60"N, 6°13′54.38"W, Fig. 1B) near the municipality of Trebujena (Spain).

2.2. Experiment design

The workflow of the experiment (Fig. 2) consisted of several steps detailed below. Data were collected at two sampling stations, respectively located in high- and low biomass biofilms in the intertidal area. Firstly, the footprints of each sample were marked on the mudflat for detection with VHR imagery. Data were gathered using a multispectral sensor at various altitudes ASL and processed to produce reflectance orthomosaics. These reflectance values were then validated using ground reference hyperspectral data (Section 2.3.1). Immediately after remote sensing spectral acquisitions, surface sediment at each sample footprint was collected using a contact-coring method (Section 2.3.2). Pigment composition analysis was performed in the laboratory using HPLC to estimate MPB biomass (Section 2.4). Subsequently, data analysis took place (Section 2.5). Firstly, various reflectance spectral indices and parameters derived from VHR reflectance data were calculated as proxies for MPB biomass at each flight altitude (Section 2.5.1). Finally, statistical analysis was conducted to evaluate associations between the various spectral indices and the *in-situ* MPB biomass data, combining both sampling stations (Section 2.5.2).

2.3. Data collection

2.3.1. Multi- & hyperspectral data collection and pre-processing

Data were collected on March 22nd 2023, during spring low tide and clear sky weather conditions. Two different sampling stations were selected in high- and low biomass biofilms in the intertidal area, named upper and lower stations respectively. We used two MicaSense RedEdge-MX dual multispectral sensors, capable of collecting ten simultaneous bands on the electromagnetic spectrum in 12-bit radiometric resolution: coastal blue (444 ± 28 nm), blue (475 ± 32 nm), green (531 ± 14 nm and 560 ± 27 nm), red (650 ± 16 nm and 668 ± 14 nm), red edge (705 ± 10 nm, 717 ± 12 nm and 740 ± 18 nm) and near-infrared (NIR, 842 ± 57 nm). This sensor includes its own downwelling light sensor (DLS) with a built-in GPS to control light conditions and solar angle changes during flight. In addition, radiometric calibration of raw pixel values into reflectance was performed with the included calibration panel (RP04-1924106-OB), which was systematically photographed just before data acquisition.

The quadcopter DJI Matrice 300 (M300, Sup. Mat. Fig. A) carried one of the multispectral sensors to conduct two different UAV surveys at 20 m altitude (one for each sampling station), the minimum flight altitude for waypoint flight planning, using the universal ground control system (UgCS) client mission planning software (SPH Engineering, Latvia, v.4.2.156) and achieving a GSD of 9.4 mm/px. Flight parameters considered 80–75 % front and side overlap and were maintained uniformly throughout the entire study area due to the MicaSense's own terrain following tool. To cover a larger area and both riverbanks, another flight was conducted at 100 m altitude (GSD of 68 mm/px) considering 80–75 % front and side overlap, respectively. Finally, individual UAV multispectral captures were taken by holding the UAV during a manual flight (without a waypoint plan), changing flight altitudes ASL to 3.5 m (GSD of 0.8 mm/px), 4.7 m (GSD of 1.1 mm/px), 6.6 m (GSD of 2.7 mm/px), 11.1 m (GSD of 4.2 mm/px), 13.8 m (GSD of 6.3 mm/px), 15.8 m (GSD of 7.1 mm/px), and 17.6 m (GSD of 8.4 mm/px). Spanish and European civil aviation regulations were followed during all UAV operations. To achieve the highest possible spatial resolution, the second multispectral sensor was also held in a small case supported by two PVC poles (Sup. Mat. Fig. A), enabling the manual execution of a waypoint plan at 1 m altitude (GSD of 0.3 mm/px) with sufficient front and side overlap between subsequent captures. Finally, a hyperspectral spectroradiometer (ASD HandHeld2, Sup. Mat. Fig. A) was employed to acquire direct *in-situ* field reflectance measurements in the 325–1075 nm spectral range over each footprint of each sample for both sampling stations (upper and lower intertidal). The hyperspectral reflectance was used for validation purposes.

The software Agisoft Metashape v.1.8.4 (Agisoft LLC, St. Petersburg, Russia) was used for processing all the waypoint flights, using a structure from motion (SfM) photogrammetric technique to generate reflectance orthomosaics for each multispectral band. After radiometric calibration of raw pixels using the calibration panel, all UAV captures were aligned with the highest possible accuracy setting to create a "3D dense cloud". This cloud was used for interpolating a digital elevation model (DEM), serving as a reference surface to produce a final reflectance orthomosaic. Individual captures taken at altitudes ranging from 3.2 m to 18 m ASL, underwent processing following the MicaSense image processing tutorial (MicaSense, 2022) to extract reflectance values, and were accurately georeferenced using the workflow provided by Román et al. (2024). The resulting orthomosaics and individual captures were projected to WGS84 UTM Zone 29 N coordinate system.

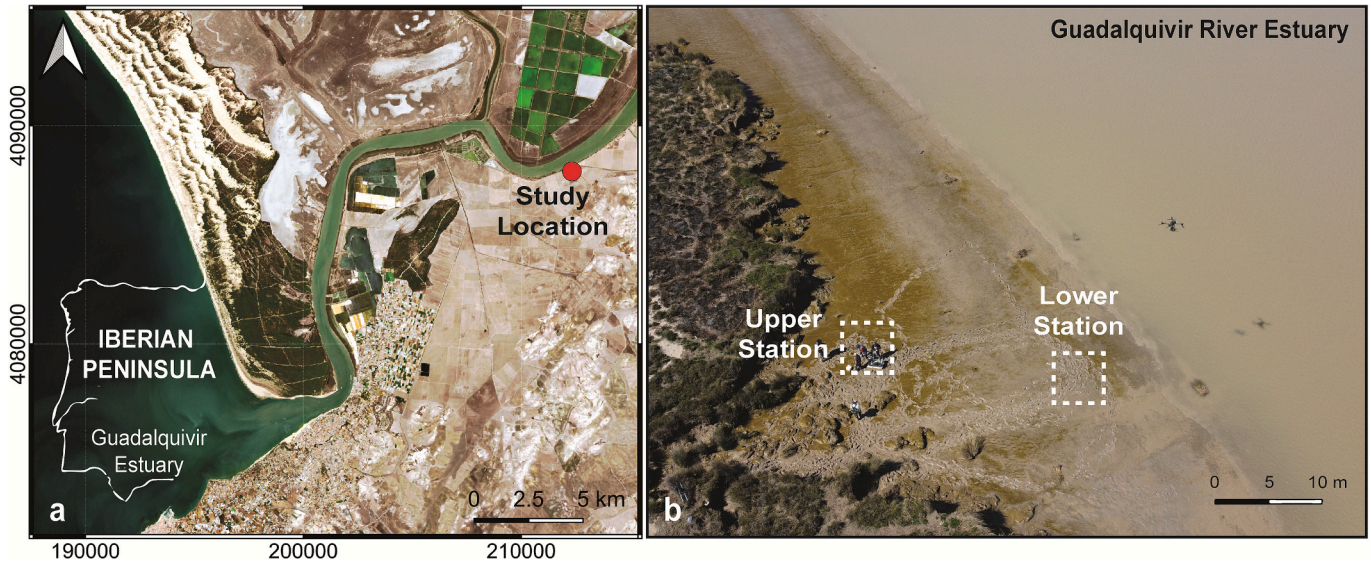

Fig. 1. (A) Sentinel-2 satellite red-green-blue (RGB) composite image captured on September 13th 2023 over the Guadalquivir Estuary, showing the location of the study site. **(B)** UAV aerial photography of the sampling stations located in high- and low biomass biofilms in the intertidal area respectively, captured during the experiment on the mudflats. In the high-biomass biofilm, MPB formed bright brown biofilms, which are characteristic of diatoms.

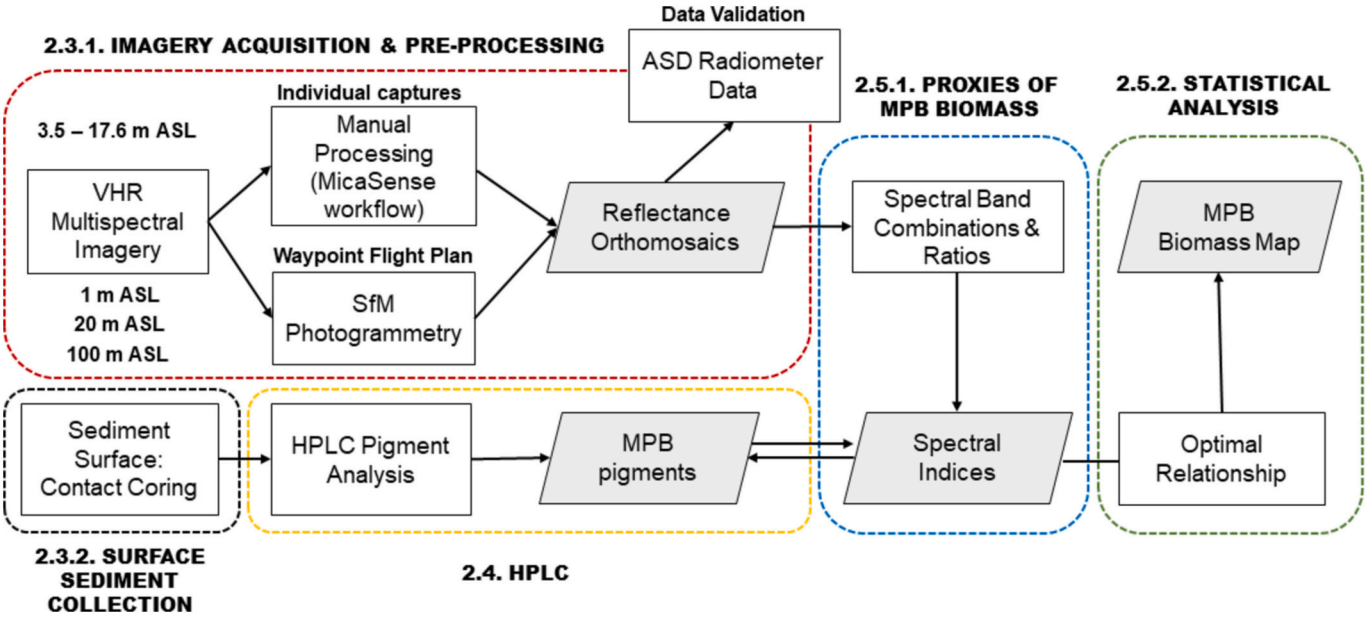

Fig. 2. Experimental workflow. Rectangular white boxes indicate processes, while rhomboid grey boxes indicate products derived from these processes.

2.3.2. *Surface sediment collection: contact-coring*

Following UAV and ASD spectral acquisitions, surface sediment was collected at each sampling station using a contact corer method. The top 2 mm of *in-situ* sediment were frozen with liquid nitrogen on a metal surface of 56 mm in diameter (Ford and Honeywill, 2002). Samples were kept in liquid nitrogen in the field, and stored at −80 °C while awaiting subsequent pigment extraction and analysis. We sampled 18 cores in the upper station and 12 cores in the lower station using a regular grid, where the rows were marked with letters in alphabetical order, while the columns were numbered starting from 1. Photographs of the surface sediment sampling with this technique are provided in Supplementary Materials Fig. A.

2.4. *Pigment analysis by high-performance liquid chromatography*

Pigment composition and biomass were estimated using high-performance liquid chromatography (HPLC), following the method described by Mantoura and Llewellyn (1983) and adapted by Méléder et al. (2003a). The HPLC device (Alliance HPLC System, Waters) was connected to an inverse-phase C-18 separating column (SunFire C-18 Column, 100 Å, 3.5 μm, 2.1 mm × 50 mm, Waters), which was preceded by a precolumn (VanGuard 3.9 mm × 5 mm, Waters), a photodiode array detector (2998 PDA), and a fluorimeter (Ex: 425 nm, Em: 655 nm; RF-20 A, SHIMADZU).

Samples were freeze-dried and weighted before initiating the HPLC analysis protocol. Initially, pigments were extracted on 0.5 g of dried sediment, by adding a specified volume of extraction solvent (95 % methanol buffered to 2 % ammonium acetate, at 4 °C) containing an internal standard (trans-β-Apo-8′-carotenal, 10,810, Sigma-Aldrich), that was vortexed for 30 s and then placed at −20 °C for 15 min. The supernatant containing pigments was recovered after centrifugation (4528 ×*g*, at 4 °C for 1 min), filtered through a 0.45 μm filter, and transferred into a brown vial for analyses. The concentration of each pigment was determined using a calibration curve diagram created with external pigment standards (DHI LAB products, Hørsholm, Denmark). The pigment content of the biofilm was expressed in surface concentration (mg m^{-2}) and included the main MPB pigments: chlorophyll-a (Chl-a), chlorophyll-c (Chl-c), diadinoxanthin (DD), diatoxanthin (DT), fucoxanthin (Fuco).

2.5. *Data analysis*

2.5.1. *Proxies of microphytobenthos pigments biomass*

Reflectance spectral indices have frequently been used as an approximation for benthic MPB pigments biomass, without undergoing additional conversion to chlorophyll-a to minimise potential estimation errors. These biological indicators are generally calculated as simple reflectance band ratios or normalized differences between NIR and visible bands. In this study, the commonly used NDVI was calculated using the UAV-based retrievals of surface reflectance in the NIR (840 nm or 740 nm) and red (668 nm) bands (Rouse et al., 1974, Eq. (1)). In addition, an adaptation of the MPBI index proposed by Méléder et al. (2010) was also calculated (Launeau et al., 2018), which combines the blue (475 nm), green (560 nm), and red (668 nm) bands (Eq. (2)).

$$\mathrm{NDVI} = \frac{(R(\mathrm{NIR}) - R(\mathrm{red}))}{(R(\mathrm{NIR} + R(\mathrm{red}))} \quad (1)$$

$$\mathrm{MPBI} = \frac{(2 \times R(\mathrm{green}))}{(R(\mathrm{blue}) + R(\mathrm{red}))} - 1 \quad (2)$$

2.5.2. *Statistical analysis*

To assess the relationship between Pigment quantity (Chl-a and Chl-c) with different reflectance based spectral indices ($NDVI_{840}$, $NDVI_{740}$ and MPBI), generalised linear mixed effect models (GLMMs) were used. Models were fit using R programming language and 'lme4' package (Bates et al., 2015; R Core Team, 2023). Response metrics (Chl-a and Chl-c) were assessed as a function of $NDVI_{840}$, $NDVI_{740}$ and MPBI, with sample zone as a random factor. A gamma distribution was used for response variables due to their continuous positive nature. Sample *vs* fitted residuals, quartile-quartile and spatial autocorrelation of samples were assessed visually, to ensure assumptions of the models were met.

This model was selected as it accounts for the disparity between the values observed at different sampling stations (low *vs* high MPB biomass, without considering intermediate biomass values). A map of the chlorophyll concentrations was created from the application of the GLMM.

3. Results

3.1. Pigmentary composition and reflectance spectra

Five liposoluble pigments (2 chlorophylls and 3 carotenoids) were identified by HPLC in each of the contact cores collected in this study, both in the upper station and in the lower station (Supplementary Table A). Three pigments characteristic of diatoms, Chl-c, DD, and Fuco were detected in all samples, while there was no chlorophyll-b, excluding the presence of euglenids. DT was also detected but at low concentrations compared to the major pigments mentioned earlier. Among the measured pigments, Chl-a and Chl-c were used as indicators of MPB biomass. The mean Chl-a concentration was significantly higher in the high biomass biofilm (53.59 ± 8.94 mg m^{-2} in average, over a range from 33.77 to 69.44 mg m^{-2}) than in the low biomass biofilm (31.30 ± 8.39 mg m^{-2} in average, over a range from 18.70 to 42.89 mg m^{-2}). Chl-c concentration was also higher in the upper station (ranging from 3.71 to 7.19 mg m^{-2}), than in the lower station (ranging from 2.13 to 4.34 mg m^{-2}).

The average reflectance spectra measured in the upper station and the lower station were compared between sensors and flight heights (Fig. 3). The spectral responses of the MicaSense multispectral sensor were consistent with the measurements from the ASD HandHeld2 hyperspectral spectroradiometer, with an offset of about 2 % observed for the low biomass biofilm. At different altitudes ASL (provided that the footprint of each contact core could be visually detected in the reflectance maps mosaicked with UAV data), there were no differences in the shape and magnitude of the MPB spectral signature between 1 and 20 m. The Chl-a absorption band, around 675 nm, was detectable with the spectral resolution provided by both the multispectral and hyperspectral sensors, while the Chl-c absorption at 632 nm was only visible in the hyperspectral reflectance data. Furthermore, noticeable changes in the reflectance spectral slope (more pronounced in the lower biomass biofilm) around 500 and 550 nm are associated with the concentration of DD + DT and Fuco, respectively. The higher concentrations in pigment biomass in the upper station also manifested in a reflectance signature with more pronounced absorption peaks than in the case of the lower station, which presented a flatter reflectance spectral shape.

3.2. Optimal aerial sampling strategy for mapping microphytobenthos biofilms

NDVI maps were obtained for each of the ASL altitudes tested in this experiment, aiming to find the optimal ASL flight altitude for detecting the contact cores footprints on the MPB biofilms (Fig. 4). In this study, different GSDs were achieved, ranging from 0.3 mm per pixel at 1 m to 9.4 mm per pixel at 20 m for the multispectral orthomosaic. Contact core footprints can be clearly distinguished up to an ASL of 11.1 m. Beyond this flight altitude, only larger features can be clearly identified, making it more challenging to cover all the pixels within each contact core footprint and leading to potential increase in error due to the inclusion of pixels that are outside the contact core. Moreover, the MicaSense multispectral sensor does not allow for the execution of waypoint flight plans with a pre-defined overlapping below 20 m ASL, thus manual capture would be a valid technique for experiments such as the one carried out in this study, whereas it would not be feasible for covering large areas as with flights conducted at 20 m or 100 m ASL. With the use of a small case supported by two PVC poles to maintain the multispectral sensor at 1 m ASL, the maximum possible spatial resolution has been achieved, thus enabling an accurate identification of the contact cores footprint. In addition, the minimal differences in the shape and magnitude of the spectral signature of each contact core at the different tested flight altitudes (Fig. 3) indicate that the spectra measured at 1 m ASL can be considered as spectrally representative for the generation of subsequent calibration models.

3.3. Spectral indices as a proxy of microphytobenthos biomass

Several spectral indices have been calculated from various combinations of the multispectral reflectance bands, especially considering the spectral band influenced by Chl-a absorption peak around 675 nm. Fig. 5 displays the results of calculating these indices from the corresponding reflectance maps with the UAV flight orthomosaic at 20 m ASL. Regarding the NDVI (for all bands in the NIR range used), values ranging between 0.4 and 0.7 were obtained for the MPB in the footprints of the contact cores sampled in the upper station. In the case of the lower station, NDVI values did not exceed 0.15. In addition, for the MPBI index, negative values were obtained in low MPB biomass zones, while these values ranged between 0.9 and 1.2 in high biomass areas on the upper station.

This information can be observed with greater precision in the

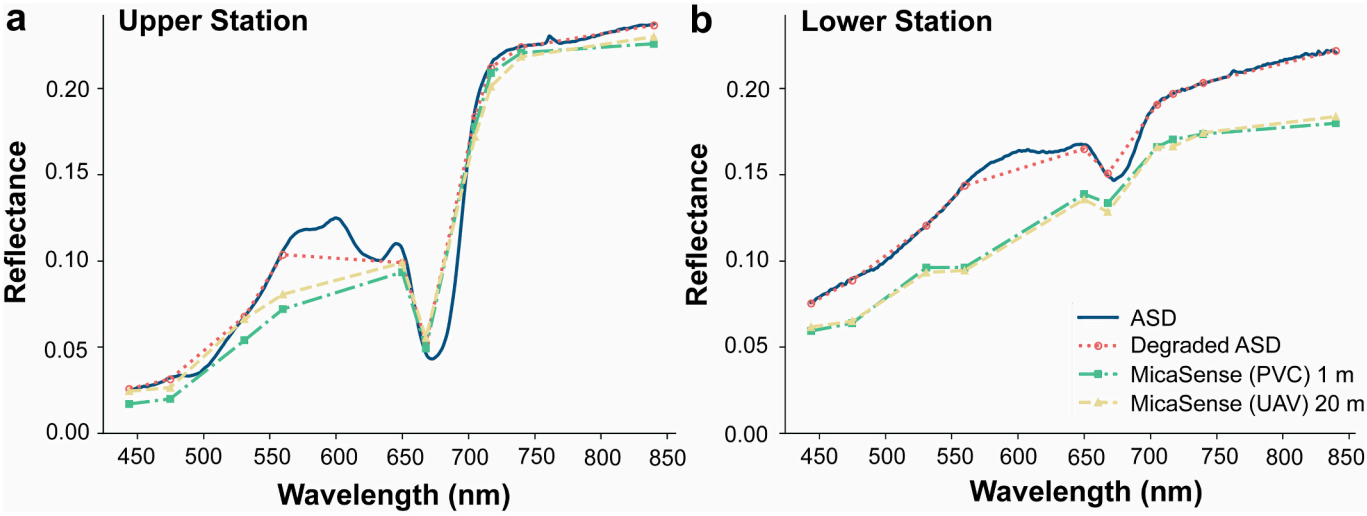

Fig. 3. Reflectance spectra measured with the multispectral sensor equipped on the UAV at 20 m, and the small case at 1 m, with the ASD spectroradiometer, and with the ASD degraded to the spectral resolution of the multispectral sensor, for **(A)** high biomass biofilm in the upper station, and **(B)** low biomass biofilm in the lower station. The plotted reflectance spectrum represents the average of the sampled spectra for each contact core at every sampling station.

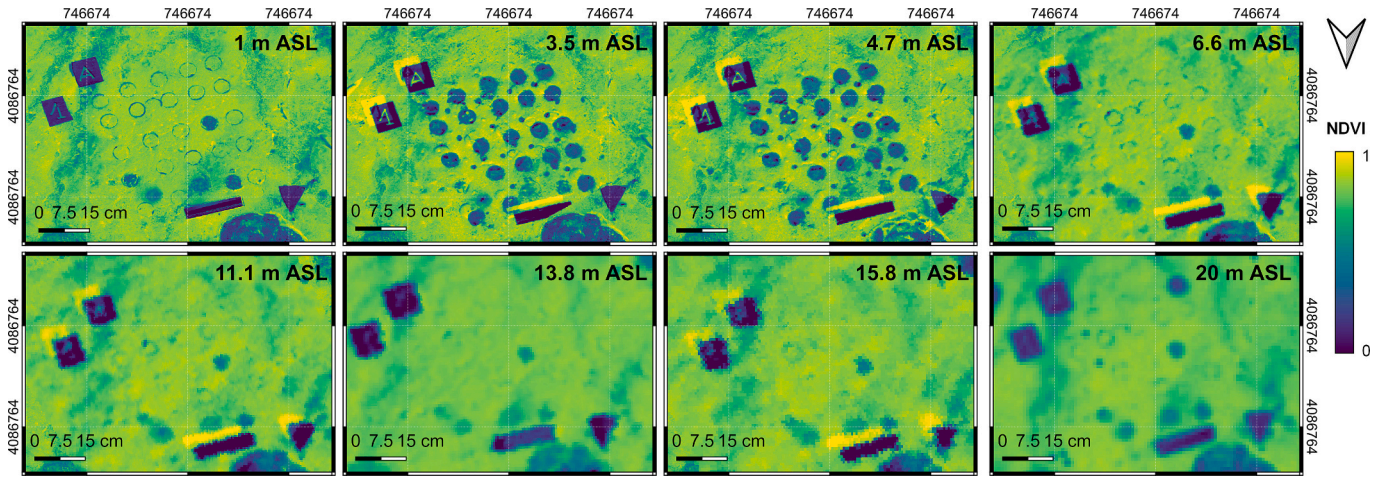

Fig. 4. Close-up of the upper station contact core footprints at different altitudes. NDVI maps were calculated using the NIR band at 840 nm at different altitudes ASL. Note that 1 m ASL corresponds to the multispectral sensor held with the small case, and that captures taken at 3.5 m and 4.7 m ASL took place, unlike the others, after sampling the sediment by contact cores.

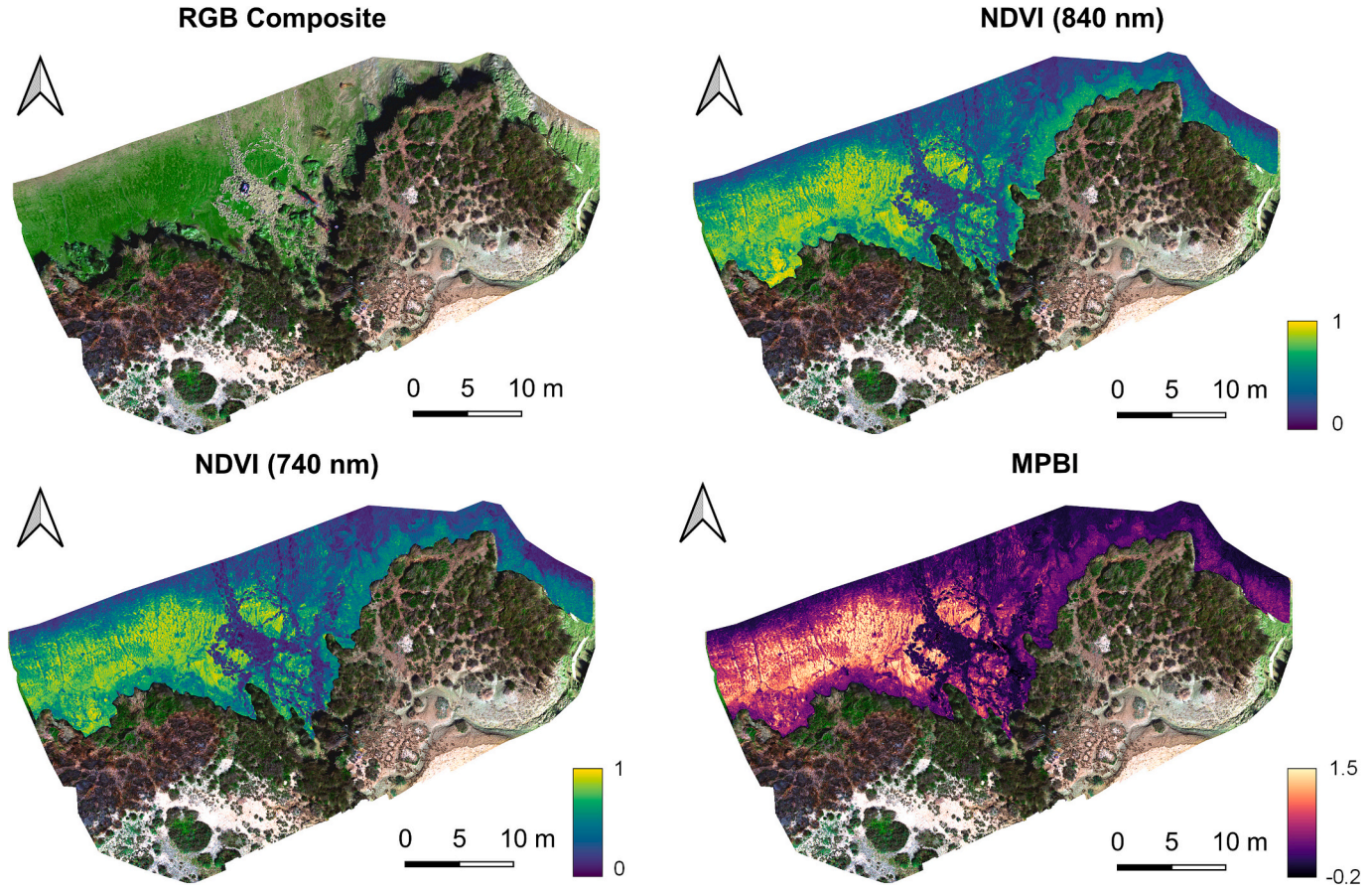

Fig. 5. RGB composite (bands red 668 nm, green 560 nm and blue 475 nm) and spectral indices (NDVI and MPBI) applied to the multispectral UAV flight at 20 m ASL showing MPB biofilms at the mudflat surface.

detailed visualisation of the sampling stations at both the higher and lower biomass biofilm areas, merged with the captures taken by holding the sensor at 1 m ASL (Fig. 6). All the cores from the upper station were sampled in a dense biofilm with averaged $NDVI_{840} > 0.60$. The lower station had a few MPB biomass patches, but most of the cores were sampled in low biomass areas with $NDVI_{840} < 0.18$ (except for a couple of contact cores (C1 and D1) located on visible patches of MPB with $NDVI_{840}$ around 0.36, which were considerably higher than the rest).

GLMMs were developed between each of the spectral indices calculated as a proxy of MPB biomass at 1 m ASL and the *in-situ* concentrations of both chlorophylls measured with HPLC in each of the contact cores, showing a significant positive relationship between Chl-a and Chl-c for all spectral indices (Fig. 7, Table 1).

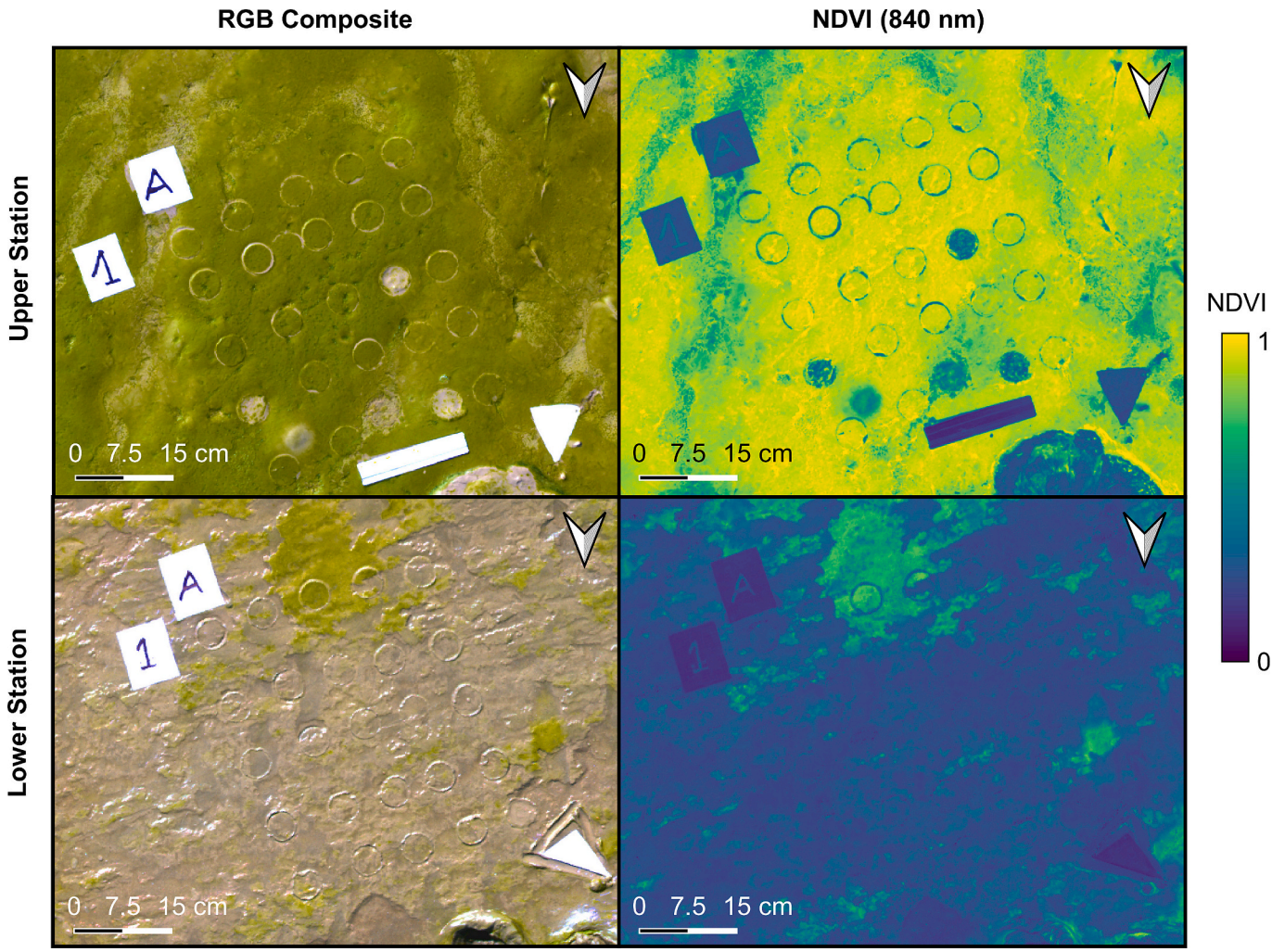

Fig. 6. Detailed view of the contact cores sampling stations in both the upper station (top panels) and the lower station (bottom panels). RGB (left) and $NDVI_{840}$ (right) images while holding the multispectral sensor at 1 m ASL. Note that three cores in the upper station were already sampled (A4, D3 and D5).

3.4. Spatial distribution of microphytobenthos biomass over the whole mudflats

The GLMM-generated enabled the mapping of MPB biomass distribution, revealing significant spatial variations related to bathymetric levels (upper *vs* lower stations) on both shores of the Guadalquivir River estuary (Fig. 8). A map showing the range of differences between the upper and lower limits of MPB biomass detection using this model is also presented in Fig. 8. In the intertidal zone on the Trebujena shore, the model predicts a decrease in biomass from areas near the fringe of the river marshes with terrestrial vegetation (where the highest Chl-a concentration range from 40 to 55 mg m^{-2}) toward the area closer to the river (Chl-a concentration decreasing from 30 to ~0 mg m^{-2}). In contrast, on the tidal flats of Doñana National Park on the opposite shore, higher values were observed near the river. The concentrations decreased in the middle intertidal but increased again near the upper terrestrial vegetation. In both areas, MPB exhibited longitudinal spatial structures parallel to the shorelines.

4. Discussion

The monitoring of MPB spatio-temporal variations is essential for estimating the health and ecological status of estuarine systems, due to its potential as a biological quality indicator (Trobajo and Sullivan, 2010) and as a carbon sequestrator in the context of climate change mitigation (Middelburg et al., 2000; Oakes and Eyre, 2014). Spatial distribution maps of MPB biomass can be used for a range of purposes from the development of biogeochemical models to estuarine management policies (Blackford, 2002; Brito et al., 2013). Various satellite imagery products covering a wide range of spatial and spectral resolutions have been used for monitoring these intertidal photo-autotrophic communities (*e.g.* Daggers et al., 2020a; Haro et al., 2022; Méléder et al., 2020; Oiry and Barillé, 2021), but the satellite pixel size remains insufficient for analysing ecological and biogeochemical processes at a local scale as for establishing precise quantitative relationships based on concomitant field measurements. This work represents one of the few approaches to study of MPB biofilms through multispectral imagery using UAVs (*e.g.* Brunier et al., 2022; Douglas et al., 2023, 2024; Launeau et al., 2018). In fact, to our knowledge, this could be considered the first UAV-based monitoring of the autotrophic community in the intertidal zone that combines collected spectral data with field measurements of MPB pigment composition using HPLC.

4.1. Technical constraints

The workflow developed in this study has been tested at different flight altitudes to be spatially consistent with a 4.5 cm diameter contact corer sampling the top 2 mm of sediment (Ford and Honeywill, 2002). Firstly, flights conducted at 20 m and 100 m ASL demonstrated the potential of UAV remote sensing for high-resolution monitoring of MPB

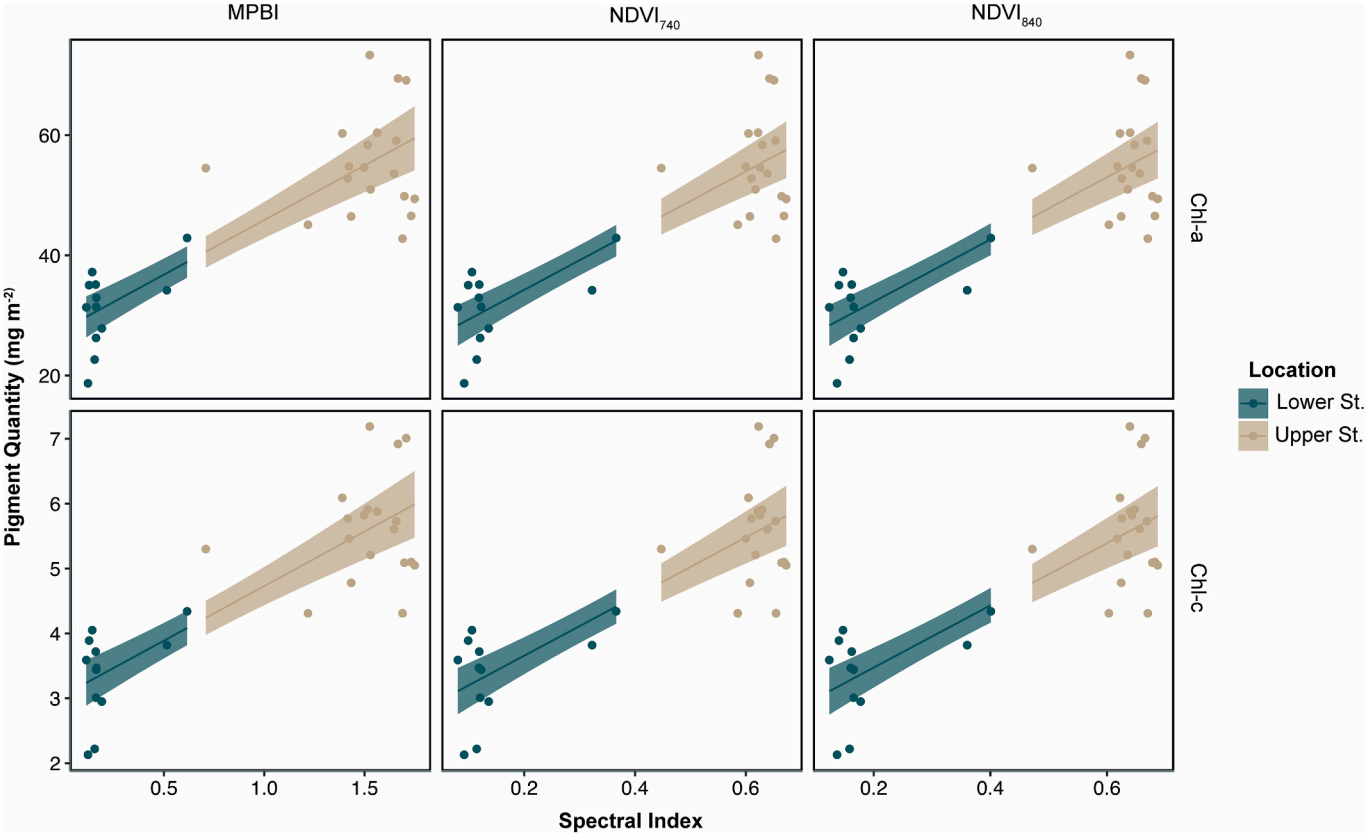

Fig. 7. MPB biomass (Chl-a and Chl-c) as a function of the calculated spectral indices at 1 m ASL. Coloured lines show model estimates with 95 % confidence intervals displayed by shading. A detailed statistical assessment is provided in Table 1.

Table 1
Generalised Linear model outputs for the Quantity of Pigment (Chl-a and Chl-c) in relation to NDVI (740 and 840) and MPBI. The term "Intercept" refers to the estimated value of the dependent variable (in this case, the concentration of chlorophyll-a or chlorophyll-c) when all other independent variables are equal to 0. Bold values denote significant *p* values (<0.05) and asterick's define level of significance: $p < 0.0001 \leq 0.0001$"***"; $p < 0.001$ = "***"; $p < 0.01$ = "**"; $p < 0.05$ = "*".

Index	Term	Chlorophyll-a, $n = 30$				Chlorophyll-c, n = 30			
		Estimate	Std. Error	t value	p value	Estimate	Std. Error	t value	p value
NDVI (840)	(Intercept)	21.9	2.17	10.10	**<0.0001*****	2.52	0.227	11.10	**<0.0001*****
	Slope	51.8	5.43	9.54	**<0.0001*****	4.79	0.548	8.75	**<0.0001*****
NDVI (740)	(Intercept)	24.4	1.95	12.50	**<0.0001*****	2.75	0.205	13.40	**<0.0001*****
	Slope	49.3	5.13	9.60	**<0.0001*****	4.56	0.518	8.80	**<0.0001*****
MPBI	(Intercept)	27.7	1.82	15.20	**<0.0001*****	3.05	0.187	16.30	**<0.0001*****
	Slope	18.2	2.04	8.92	**<0.0001*****	1.68	0.201	8.38	**<0.0001*****

biofilms in intertidal zones. However, the GSD of the reflectance maps generated from these flight altitudes was insufficient to detect the contact core footprints, despite the ability to cover a spatially broader area in the study region. Moreover, the 20 m ASL has been identified as the minimum flight altitude that allows for executing a waypoint flight plan for the subsequent application of photogrammetric software to generate reflectance maps of the entire monitored intertidal zone. Below this flight altitude, the only valid technique would consist of collecting individual captures in manual flight mode, followed by processing for georeferencing and extraction of reflectance maps for each spectral band. Although there are open-source automated techniques that provide promising results (*e.g.* MicaSense, 2022; Román et al., 2024), when working with millimetric-scale GSDs, there is a significant misalignment between the different sensor bands that requires manual orthorectification to generate spectral indices and/or band composites (Fernández et al., 2021). This process is time-consuming and inefficient, as manual orthorectification also reduces the spatial resolution of the image, making it challenging to detect contact core footprints, as is the case with captures taken at 11.1 m, 13.8 m, and 15.8 m ASL (Fig. 4). Consequently, from the image processing, it is concluded that the higher the GSD, the greater the misalignment of the spectral bands, and there is a need to find an alternative that allows for the application of photogrammetric software to mosaic, georeference, align, and derive reflectance maps.

To tackle these constraints, a setup consisting of a small case supported by two PVC poles holding the multispectral sensor at an approximate height of 1 m ASL over the sampling station was used, thus overcoming the limitations in data processing mentioned earlier (Sup. Mat. Fig. A). In this way, the highest GSD possible was achieved (0.3 mm/px), which has also allowed for the establishment of quantitative relationships with pigments used as proxies of MPB biomass measured by HPLC. The relationships were obtained for a height of 1 m. It was applied at 20 m after checking the consistency of the spectral responses of the multispectral camera for the two flight heights (Fig. 3). This new approach has allowed us to precisely achieve a level of detail sufficient to overcome the limitations offered by previous attempts when seeking

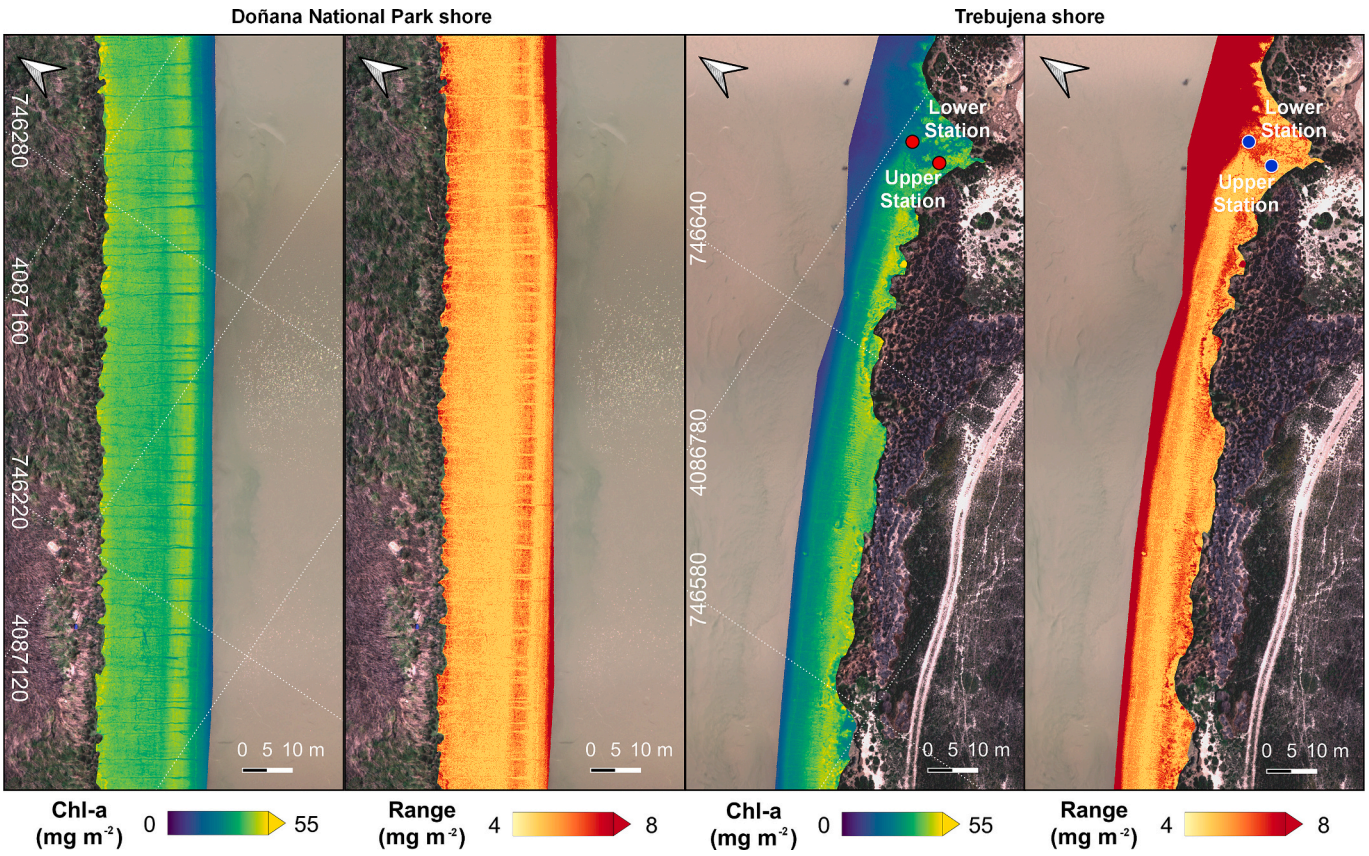

Fig. 8. Spatial distribution of benthic Chl-a concentration (mg m^{-2}) utilized as a proxy for MPB biomass in the Guadalquivir estuary in March 2023. This map was generated using the $NDVI_{740}$. A multispectral UAV orthomosaic with a spatial resolution of 6.8 cm/px was calibrated using the relationship obtained from the model illustrated in Fig. 7 and Table 1. In addition to the biomass map, the range of differences between the upper and lower 95 % confidence intervals of MPB biomass estimates using this model is presented for each river shore.

robust spatial consistency between contact-coring sampling and UAV derived spectral indexes at a millimetric scale. This will enable future work that requires a short time lag between sampling and imaging when analysing the spatial and temporal variability of MPB with the tide; a finer level of detail to detect a broader range of biomass; or detect MPB biomass production down to a maximum depth of 2 mm, an aspect hardly attainable with the spatial resolutions provided by satellite remote sensing. Furthermore, it is demonstrated that, using modelling approaches such as the one suggested in this study (Table 1), it is feasible to measure the MPB biomass with a UAV at 100 m ASL (Fig. 8). Indeed, a perspective would be to test higher flight heights using the presented models to cover a broader expanse in the intertidal areas of the Guadalquivir estuary. In addition, the methodology suggested in this study (fine spatial resolution imaging, contact-corer sampling, and GLMMs models) could be applied to different mudflats or heterogeneous ecosystems, opening up a new range of possibilities for monitoring and tracking these systems.

4.2. Spatial distribution of microphytobenthos in a southern Europe estuary

In this work, the values obtained from the combination of the multispectral sensor bands provided maximum values around ~0.7 for the NDVI and ~ 1.2 for the MPBI, higher than those obtained for other European estuaries (*e.g.* Brito et al., 2013; Daggers et al., 2020b; Van der Wal et al., 2010). However, the position and the width of spectral bands differ between sensors, and absolute values should be compared cautiously. Furthermore, the modelled Chl-a concentration range in this study (30 mg m^{-2}–55 mg m^{-2}, which corresponds to 15 μg cm^{-3}–27.5 μg cm^{-3} for a 2 mm depth contact core) was higher than that found by Pérez-Rodríguez et al. (2024) in Bonanza and Lebrija, two locations geographically close to the study site, for the same period of the year. This concentration range also exceeds those observed in the Bay of Cádiz (*e.g.* García-Robledo et al., 2016; Haro et al., 2019) and other estuarine regions around the world (Cabrita and Brotas, 2000; McTigue et al., 2015; Kwon et al., 2020), which ranged from approximately 12 μg cm^{-3} to 15 μg cm^{-3}. This study was conducted in late winter, coinciding with the seasonal MPB biomass peak in the Guadalquivir estuary (Pérez-Rodríguez et al., 2024), thereby explaining the high Chl-a concentration range. In addition, the higher biomass concentration recorded is also associated with the migration of MPB thriving on muddy sediments, such as those in the Guadalquivir estuary, into narrow photic zones with tidal range (Underwood et al., 2022).

Specifically, the highest biomass was observed near the fringe of the terrestrial vegetation, and the MPB biofilm displayed marked spatial patterns in bands parallel to the shoreline. Similar patterns were detected in the Loire estuary (Benyoucef et al., 2014) and in the Bay of Cádiz (Haro et al., 2022), where bathymetry was identified as an essential structuring variable. These bathymetric gradients suggest the effect of abiotic factors such as exposure time, which directly influences the amount of light received by these microbial communities and desiccation, nutrients that percolate from the land area, or current velocity, which is related to shear stress and ultimately erosion (Brito et al., 2013; Haro et al., 2022; Jesus et al., 2009; Koh et al., 2006; Van der Wal et al., 2010). On the other bank of the Guadalquivir River, adjacent to the Doñana National Park, the mudflat was more extensive, with a width of *ca.* 23 m compared to *ca.* 12 m at the study site. There, high biomass was observed near the terrestrial vegetation, but also in the vicinity of the river, forming a conspicuous pattern (Fig. 8). Such patterns have been described in the literature, even if they were not the main reported

result, indicating that other factors apart from those driven by the bathymetry constrain the spatial distribution of the MPB biomass (Benyoucef et al., 2014; Haro et al., 2022; Méléder et al., 2003a).

4.3. Caveats and future perspectives

The index values used to create these relationships range from 0.12 to 0.69, 0.08 to 0.67, and 0.11 to 1.75 for $NDVI_{840}$, $NDVI_{740}$, and MPBI respectively. As a result, model estimates for values outside of these ranges will yield lower confidence, as occurs in areas with higher MPB biomass, where the difference between the upper and lower limits of detection is greater, and consequently, the estimation carries higher uncertainty (Fig. 8). Similarly, values in the middle of these ranges were also scarce in this study, increasing uncertainty in that portion of the data. Future work should aim to fill these gaps in the spectral index ranges. In addition, future research should cover different spatial and temporal scales to critically assess the generalisability and broader applicability of the current relationships. Indeed, this study's perspective is to demonstrate the potential of using high-resolution multispectral data collected with UAVs to train and validate numerical models or machine learning algorithms that enable the use of Sentinel-2 imagery to reveal MPB biomass across the entire Guadalquivir estuary.

A critical process that must be considered when mapping MPB in intertidal zones is the short-scale (from minutes to hours) vertical migration of cells in the sediment (Barnett et al., 2020; Haro et al., 2019). Migration is primarily related to light and tidal variability, but other drivers can have a significant role (Consalvey et al., 2004). In this study, all measurements were taken at ±1 h around low tide when the biofilm was well established, with likely no influence of migration on the remotely-sensed biomass, as shown by Méléder et al. (2003b). Future work should take advantage of the temporal flexibility of using sensors aboard UAVs to characterise this MPB vertical migration during the first and last hours of the daytime emersion period to characterise the upward and downward migrations. New hyperspectral sensors adapted to UAV platforms can provide unprecedented spectral, spatial, and temporal resolutions that would be interesting for analysing MPB photophysiology and primary production (Méléder et al., 2018). In the Guadalquivir River estuary, MPB uniquely colonised the intertidal zone, but the vast majority of intertidal systems are composed of an assemblage of macroalgae, marine angiosperms, or vascular plants (*e.g.* Haro et al., 2022; Oiry and Barillé, 2021; Wang et al., 2018). When MPB is found with other types of intertidal vegetation, spectral indices are not the best solution. Oiry and Barillé (2021) and Haro et al. (2022) had to resort to more complex techniques based on machine learning algorithms that combine multispectral satellite bands and vegetation indices to address this significant challenge.

5. Conclusions

The innovative aspect of this work relied on the spatial consistency between contact-coring sampling at 25 cm^2 and *in-situ* spectra collected at millimetric spatial resolution. The multispectral sensor was mounted on a UAV and a hand-held platform, allowing for the establishment of quantitative relationships between reflectance spectral indices commonly used as proxies for MPB biomass and pigments (Chl-a and Chl-c) measured by HPLC. Spatial distribution maps of MPB biomass showed longitudinal structures parallel to the shore with high biomass near the fringe of the river marshes with terrestrial vegetation. These maps represent the first step toward possible synoptic MPB monitoring at the ecosystem level. Indeed, the robustness of the GLMM generated to map MPB biomass is demonstrated, successfully upscaling to 100 m ASL with UAV flight, suggesting that the next steps should focus on using satellite images or UAV flights at higher altitudes to estimate MPB contribution to carbon sequestration in the entire Guadalquivir estuary. As MPB provides many ecosystem services (Hope et al., 2019), the results of this study should encourage environmental managers and decision-makers not to omit this critical component of turbid estuarine ecosystems when assessing their status, health, and potential impact of climate change.

Supplementary data to this article can be found online at https://doi.org/10.1016/j.scitotenv.2024.177025.

CRediT authorship contribution statement

Alejandro Román: Writing – original draft, Validation, Software, Methodology, Investigation, Formal analysis, Data curation, Conceptualization. **Simon Oiry:** Writing – review & editing, Software, Methodology. **Bede F.R. Davies:** Writing – review & editing, Validation, Software, Methodology. **Philippe Rosa:** Writing – review & editing, Methodology, Data curation. **Pierre Gernez:** Writing – review & editing, Formal analysis. **Antonio Tovar-Sánchez:** Writing – review & editing, Supervision, Funding acquisition. **Gabriel Navarro:** Writing – review & editing, Methodology, Funding acquisition. **Vona Méléder:** Writing – review & editing, Supervision, Funding acquisition, Formal analysis, Conceptualization. **Laurent Barillé:** Writing – review & editing, Supervision, Investigation, Formal analysis, Conceptualization.

Funding

This study has been supported by the REWRITE project, funded through the European Union's Horizon Europe research and innovation program under grant agreement no. 101081357. This research was also possible thanks to the SAT4ALGAE project (PY20-00244) funded by Junta de Andalucía, Momentum CSIC Programme: Develop Your Digital Talent (MMT24-ICMAN-01) associated to OPECAM, the Observatorio TIAMAT project (REF: 2715/2021) from the OAPN and PROY. 2022/26. A.R. is supported by grant FPU19/04557 funded by Ministry of Universities of the Spanish Government. This work represents a contribution to CSIC Thematic Interdisciplinary Platform PTI TELEDETECT.

Declaration of competing interest

The authors declare that they have no known competing financial interests or personal relationships that could have appeared to influence the work reported in this paper.

Acknowledgements

The authors would like to thank María Nicolau and Antonio Moreno from ICMAN-CSIC (OPECAM-SEADRON Unit) for their contribution in the performance of UAV surveys.

Data availability

Data will be made available on request.

References

Barillé, L., Mouget, J.L., Méléder, V., Rosa, P., Jesus, B., 2011. Spectral response of benthic diatoms with different sediment backgrounds. Remote Sens. Environ. 115, 1034–1042. https://doi.org/10.1016/j.rse.2010.12.008.

Barnett, A., Méléder, V., Dupuy, C., Lavaud, J., 2020. The vertical migratory rhythm of intertidal microphytobenthos in sediment depends on the light photoperiod, intensity, and spectrum: evidence for a positive effect of blue wavelengths. Front. Mar. Sci. 7, 212. https://doi.org/10.3389/fmars.2020.00212.

Bates, D., Mächler, M., Bolker, B., Walker, S., 2015. Fitting linear mixed-effects models using lme4. J. Stat. Softw. 67 (1), 1–48. https://doi.org/10.18637/jss.v067.i01.

Benyoucef, I., Blandin, E., Lerouxel, A., Jesus, B., Rosa, P., Méléder, V., Launeau, P., Barillé, L., 2014. Microphytobenthos interannual variations in a north-European estuary (Loire estuary, France) detected by visible-infrared multispectral remote sensing. Estuar. Coast. Shelf Sci. 136, 43–52. https://doi.org/10.1016/j.ecss.2013.11.007.

Blackford, J.C., 2002. The influence of microphytobenthos on the northern Adriatic ecosystem: a modelling study. Estuar. Coast. Shelf Sci. 55, 109–123. https://doi.org/10.1006/ecss.2001.0890.

Blanchard, G.F., Guarini, J., Orvain, F., Sauriau, P., 2001. Dynamic behaviour of benthic microalgal biomass in intertidal mudflats. J. Exp. Mar. Biol. Ecol. 264 (1), 85–100. https://doi.org/10.1016/S0022-0981(01)00312-4.

Brito, A.C., Benyoucef, I., Jesus, B., Brotas, V., Gernez, P., Mendes, C.R., Launeau, P., Dias, M.P., Barillé, L., 2013. Seasonality of microphytobenthos revealed by remote-sensing in a south European estuary. Cont. Shelf Res. 66, 83–91. https://doi.org/10.1016/j.csr.2013.07.004.

Brotas, V., Plante-Cuny, M.R., 2003. The use of HPLC pigment analysis to study microphytobenthos communities. Acta Oecol. 24 (1), S109–S115. https://doi.org/10.1016/S1146-609X(03)00013-4.

Brunier, G., Oiry, S., Lachaussée, N., Barillé, L., Le Fouest, V., Méléder, V., 2022. A machine-learning approach to intertidal mudflat mapping combining multispectral reflectance and geomorphology from UAV-based monitoring. Remote Sens. 14 (22), 5857. https://doi.org/10.3390/rs14225857.

Caballero, I., Navarro, G., Ruiz, J., 2018. Multi-platform assessment of turbidity plumes during dredging operations in a major estuarine system. Int. J. Appl. Earth Obs. Geoinf. 68, 31–43. https://doi.org/10.1016/j.jag.2018.01.014.

Cabrita, M.T., Brotas, V., 2000. Seasonal variation in denitrification and dissolved nitrogen fluxes in intertidal sediments of the Tagus estuary, Portugal. Mar. Ecol. Prog. Ser. 202, 51–65. https://doi.org/10.3354/meps202051.

Cahoon, L.B., 1999. The role of benthic microalgae in neritic ecosystems. Oceanogr. Mar. Biol. Annu. Rev. 37, 47–86.

Consalvey, M., Paterson, D.M., Underwood, G.J.C., 2004. The ups and downs of life in a benthic biofilm: migration of benthic diatoms. Diatom Res. 19, 181–202. https://doi.org/10.1080/0269249X.2004.9705870.

Daggers, T.D., Kromkamp, J.C., Herman, P.M.J., Van der Wal, D., 2018. A model to assess microphytobenthic primary production in tidal systems using satellite remote sensing. Remote Sens. Environ. 211, 129–145. https://doi.org/10.1016/j.rse.2018.03.037.

Daggers, T.D., Van Oevelent, D., Herman, P.M.J., Boschker, H.T.S., Van der Wal, D., 2020a. Spatial variability in macrofaunal diet composition and grazing pressure on microphytobenthos in intertidal areas. Limnol. Oceanogr. Methods 65 (11), 2819–2834. https://doi.org/10.1002/lno.11554.

Daggers, T.D., Herman, P.M.J., Van der Wal, D., 2020b. Seasonal and spatial variability in patchiness of microphytobenthos on intertidal flats from Sentinel-2 satellite imagery. Front. Mar. Sci. 7, 392. https://doi.org/10.3389/fmars.2020.00392.

Douglas, T.J., Coops, N.C., Drever, M.C., 2023. UAV-acquired imagery with photogrammetry provides accurate measures of mudflat elevation gradients and microtopography for investigating microphytobenthos patterning. Sci. Remote Sens. 7, 100089. https://doi.org/10.1016/j.srs.2023.100089.

Douglas, T.J., Coops, N.C., Drever, M.C., Hunt, B.P.V., Martin, T.G., 2024. Linking microphytobenthos distribution and mudflat geomorphology under varying sedimentary regimes using unoccupied aerial vehicle (UAV)-acquired multispectral reflectance and photogrammetry. Sci. Total Environ. 942, 173675. https://doi.org/10.1016/j.scitotenv.2024.173675.

Echappé, C., Gernez, P., Méléder, V., Jesus, B., Cognie, B., Decottignies, P., Sabbe, K., Barillé, L., 2018. Satellite remote sensing reveals a positive impact of living oyster reefs on microalgal biofilm development. Biogeosciences 15, 905–918. https://doi.org/10.5194/bg-15-905-2018.

Fernández, C.I., Haddadi, A., Leblon, B., Wang, J., Wang, K., 2021. Comparison between three registration methods in the case of non-georeferenced close range of multispectral images. Remote Sens. 13 (3), 396. https://doi.org/10.3390/rs13030396.

Ford, R.B., Honeywill, C., 2002. Grazing on intertidal microphytobenthos by macrofauna: is pheophorbide a useful marker? Mar. Ecol. Prog. Ser. 229, 33–42. https://doi.org/10.3354/meps229033.

Frakenbach, S., Ezequiel, J., Plecha, S., Goessling, J.W., Vaz, L., Kühl, M., Miguel Dias, J., Vaz, N., Seródio, J., 2020. Synoptic spatio-temporal variability of the photosynthetic productivity of microphytobenthos and phytoplankton in a tidal estuary. Front. Mar. Sci. 7, 170. https://doi.org/10.3389/fmars.2020.00170.

García-Robledo, E., Bohórquez, J., Corzo, A., Jiménez-Arias, J.L., Papaspyrou, S., 2016. Dynamics of inorganic nutrients in intertidal sediments: porewater, exchangeable, and intracellular pools. Front. Microbiol. 7, 761. https://doi.org/10.3389/fmicb.2016. 00761.

Guarini, J., Blanchard, G.F., Gros, P., 2000. Quantification of the microphytobenthic primary production in European intertidal mudflats – a modelling approach. Cont. Shelf Res. 20 (12–13), 1771–1788. https://doi.org/10.1016/S0278-4343(00)00047-9.

Guarini, J.M., Blanchard, G.F., Bacher, C., Gros, P., Riera, P., Richard, P., Gouleau, D., Galois, R., Jean, P., Sauriau, P.G., 1998. Dynamics of spatial patterns of microphytobenthic biomass: inferences from a geostatistical analysis of two comprehensive surveys in Marennes-Oléron Bay (France). Mar. Ecol. Prog. Ser. 166, 131–141. https://doi.org/10.3354/meps166131.

Haro, S., Bohórquez, J., Lara, M., García-Robledo, E., González, C.J., Crespo, J.M., Papaspyrou, S., Corzo, A., 2019. Diel patterns of microphytobenthic primary production in intertidal sediments: the role of photoperiod on the vertical migration circadian rhythm. Sci. Rep. 9, 13376. https://doi.org/10.1038/s41598-019-49971-8.

Haro, S., Jesus, B., Oiry, S., Papaspyrou, S., Lara, M., González, C.J., Corzo, A., 2022. Microphytobenthos spatio-temporal dynamics across an intertidal gradient using random Forest classification and Sentinel-2 imagery. Sci. Total Environ. 804, 149983. https://doi.org/10.1016/j.scitotenv.2021.149983.

Hope, J.A., Paterson, D.M., Thrush, S.F., 2019. The role of microphytobenthos in soft-sediment ecological networks and their contribution to the delivery of multiple ecosystem services. J. Ecol. 108 (3), 815–830. https://doi.org/10.1111/1365-2745.13322.

Jacobs, P., Pitarch, J., Kromkamp, J.C., Philippart, C.J.M., 2021. Assessing biomass and primary production of microphytobenthos in depositional coastal systems using spectral information. PLoS One 16 (7), e0246012. https://doi.org/10.1371/journal.pone.0246012.

Jesus, B., Mendes, C.R., Brotas, V., Paterson, D.M., 2006. Effect of sediment type on microphytobenthos vertical distribution: modelling the productive biomass and improving ground truth measurements. J. Exp. Mar. Biol. Ecol. 332 (1), 60–74. https://doi.org/10.1016/j.jembe.2005.11.005.

Jesus, B., Brotas, V., Ribeiro, L., Mendes, C.R., Cartaxana, P., Paterson, D.M., 2009. Adaptations of microphytobenthos assemblages to sediment type and tidal position. Cont. Shelf Res. 29, 1624–1634. https://doi.org/10.1016/j.csr.2009.05.006.

Jesus, B., Rosa, P., Mouget, J.L., Méléder, V., Launeau, P., Barillé, L., 2014. Spectral-radiometric analysis of taxonomically mixed microphytobenthic biofilms. Remote Sens. Environ. 140, 196–205. https://doi.org/10.1016/j.rse.2013.08.040.

Jiménez-Arias, J.L., Morris, E., Rubio-de-Inglés, M.J., Peralta, G., García-Robledo, E., Corzo, A., Papaspyrou, S., 2020. Tidal elevation is the key factor modulating burial rates and composition of organic matter in a coastal wetland with multiple habitats. Sci. Total Environ. 724 (1), 138205. https://doi.org/10.1016/j.scitotenv.2020.138205.

Koh, C.H., Khim, J.S., Araki, H., Yamanishi, H., Mogi, H., Koga, K., 2006. Tidal resuspension of microphytobenthic chlorophyll a in a Namura mudflat, Saga, Ariake Sea, Japan: flood-ebb and spring-neap variations. Mar. Ecol. Prog. Ser. 312, 85–100. https://doi.org/10.3354/meps312085.

Kromkamp, J.C., Morris, E.P., Forster, R.M., Honeywill, C., Hagerthey, S., Paterson, D.M., 2006. Relationship of intertidal surface sediment chlorophyll concentration to hyperspectral reflectance and chlorophyll fluorescence. Estuar. Coasts 29 (2), 183–196.

Kwon, B.O., Kim, H., Noh, J., Lee, S.Y., Nam, J., Khim, J.S., 2020. Spatiotemporal variability in microphytobenthic primary production across bare intertidal flat, saltmarsh, and mangrove forest of Asia and Australia. Mar. Pollut. Bull. 151, 110707. https://doi.org/10.1016/j.marpolbul.2019.110707.

Launeau, P., Méléder, V., Verpoorter, C., Barillé, L., Kazemipour-Ricci, F., Giraud, M., Jesus, B., Le Menn, E., 2018. Microphytobenthos biomass and diversity mapping at different spatial scales with a hyperspectral optical model. Remote Sens. 10, 716. https://doi.org/10.3390/rs10050716.

MacIntyre, H.L., Geider, R.J., Miller, D.C., 1996. Microphytobenthos: the ecological role of the "secret garden" of unvegetated, shallow-water marine habitats. I. Distribution, abundance and primary production. Estuaries 19, 186. https://doi.org/10.2307/1352224.

Mantoura, R.F.C., Llewellyn, C.A., 1983. The rapid determination of algal chlorophyll and carotenoid pigments and their breakdown products in natural waters by reverse-phase high-performance liquid chromatography. Anal. Chim. Acta 151, 297–314. https://doi.org/10.1016/S0003-2670(00)80092-6.

McTigue, N.D., Bucolo, P., Liu, Z., Dunton, K.H., 2015. Pelagic-benthic coupling, food webs, and organic matter degradation in the Chukchi Sea: insights from sedimentary pigments and stable carbon isotopes. Limnol. Oceanogr. 60, 429–445. https://doi.org/10.1002/lno.10038.

Méléder, V., Barillé, L., Launeau, P., Carrère, V., Rincé, Y., 2003a. Spectrometric constraint in analysis of benthic diatom biomass using monospecific cultures. Remote Sens. Environ. 88, 386–400. https://doi.org/10.1016/j.rse.2003.08.009.

Méléder, V., Launeau, P., Barillé, L., Rincé, Y., 2003b. Microphytobenthos assemblage mapping by spatial visible-infrared remote sensing in a shellfish ecosystem. C. R. Biol. 326 (4), 377–389.

Méléder, V., Barillé, L., Rincé, Y., Morançais, M., Rosa, P., Gaudin, P., 2005. Spatio-temporal changes in microphytobenthos structure analysed by pigment composition in a macrotidal flat (Bourgneuf Bay, France). Mar. Ecol. Prog. Ser. 297, 83–99. https://doi.org/10.3354/meps297083.

Méléder, V., Launeau, P., Barillé, L., Combe, J.P., Carrère, V., Jesus, B., Verpoorter, C. (2010) Hyperspectral imaging for mapping microphytobenthos in coastal areas. *In: Geomatic Solutions for Coastal Environment*, 4. DOI:10.13140/RG.2.1.2559.0808.

Méléder, V., Jesus, B., Barnett, A., Barillé, L., Lavaud, J., 2018. Microphytobenthos primary production estimated by hyperspectral reflectance. PLoS One 13 (5), e0197093. https://doi.org/10.1371/journal.pone.0197093.

Méléder, V., Savelli, R., Barnett, A., Polsenaere, P., Gernez, P., Cugier, P., Lerouxel, A., Le Bris, A., Dupuy, C., Le Fouest, V., Lavaud, J., 2020. Mapping the intertidal Microphytobenthos gross primary production part I: coupling multispectral remote sensing and physical modeling. Front. Mar. Sci. 7, 1–16. https://doi.org/10.3389/fmars.2020.00520.

MicaSense. Image Processing Tutorials. (2022) Available online: https://github.com/micasense/imageprocessing/actions (accessed on 27 November 2022).

Middelburg, J.J., Barranguet, C., Boschker, H.T.S., Herman, P.M.J., Moens, T., Heip, C.H.R., 2000. The fate of intertidal microphytobenthos carbon: an in situ ^{13}C-labeling study. Limnol. Oceanogr. Methods 45 (6), 1224–1234.

Miller, D.C., Geider, R.J., MacIntyre, H.L., 1996. Microphytobenthos: the ecological role of the "secret garden" of unvegetated, shallow-water marine habitats. II. Role in sediment stability and shallow-water food webs. Estuaries 19, 202–212. https://doi.org/10.2307/1352225.

Miró, J.M., Megina, C., Donázar-Aramendía, I., García-Gómez, J.C., 2022. Effects of maintenance dredging on the macrofauna of the water column in a turbid estuary. Sci. Total Environ. 806 (3), 151304. https://doi.org/10.1016/j.scitotenv.2021.151304.

Oakes, J.M., Eyre, B.D., 2014. Transformation and fate of microphytobenthos carbon in subtropical, intertidal sediments: potential for long-term retention revealed by ^{13}C-labeling. Biogeosciences 11, 1927–1940. https://doi.org/10.5194/bg-11-1927-2014.

Oiry, S., Barillé, L., 2021. Using Sentinel-2 satellite imagery to develop microphytobenthos-based water quality indices in estuaries. Ecol. Indic. 121, 107184. https://doi.org/10.1016/j.ecolind.2020.107184.

Orvain, F., Lefebvre, S., Montepini, J., Sébire, M., Gangnery, A., Sylvand, B., 2012. Spatial and temporal interaction between sediment and microphytobenthos in a temperate estuarine macro-intertidal bay. Mar. Ecol. Prog. Ser. 458, 53–68. https://doi.org/10.3354/meps09698.

Otani, S., Endo, T., 2018. CO_2 flux in tidal flats and salt marshes. In: Kuwae, T., Hori, M. (Eds.), Blue Carbon in Shallow Coastal Ecosystems. Springer, Singapore. https://doi.org/10.1007/978-981-13-1295-3_8.

Park, J., Lee, H., Asselman, J., Janssen, C., Depuydt, S., De Saeger, J., Friedl, T., Sabbe, K., Vyverman, W., Philippart, C.J.M., Pitarch, J., Heynderickx, P.M., Wu, D., Ronsse, F., De Neve, W., Pandey, L.K., Park, J.T., Han, T., 2024. Harnessing the power of tidal flat diatoms to combat climate change. Crit. Rev. Environ. Sci. Technol. 1-22. https://doi.org/10.1080/10643389.2024.2315004.

Pérez-Rodríguez, V., Corzo, A., Papaspyrou, S., Garcia-Robledo, E., 2024. Benthic metabolism and nutrient dynamics of an hyperturbid and hypernutrified estuary. Front. Mar. Sci. 11. https://doi.org/10.3389/fmars.2024.1389673.

Pinckney, J.L., 2018. A mini-review of the contribution of benthic microalgae to the ecology of the continental shelf in the South Atlantic bight. Estuar. Coasts 41, 2070–2078. https://doi.org/10.1007/s12237-018-0401-z.

R Core Team (2023) R: A Language and Environment for Statistical Computing. Vienna, Austria: R Foundation for Statistical Computing. Available online: https://www.R-project.org/ (accessed 08-07-2024).

Reddin, C.J., Decottignies, P., Bacouillard, L., Barillé, L., Dubois, S.F., Echappé, C., Gernez, P., Jesus, B., Méléder, V., Nätscher, P.S., Turpin, V., Zeppilli, D., Zwerschke, N., Brind'Amour, A., Cognie, B., 2022. Extensive spatial impacts of oyster reefs on an intertidal mudflat community via predator facilitation. Commun. Biol. 5, 250. https://doi.org/10.1038/s42003-022-03192-4.

Ribeiro, L., Benyoucef, I., Poulin, M., Jesus, B., Rosa, P., Méléder, V., Du, G., Barillé, L., 2021. Spatio-temporal variation of microphytobenthos biomass, diversity and assemblage structure in the Loire estuary, France. Aquat. Microb. Ecol. 87, 61–77. https://doi.org/10.3354/ame01971.

Román, A., Heredia, S., Windle, A.E., Tovar-Sánchez, A., Navarro, G., 2024. Enhancing georeferencing and mosaicking techniques over water surfaces with high-resolution unmanned aerial vehicle (UAV) imagery. Remote Sens. 16 (2), 290. https://doi.org/10.3390/rs16020290.

Rouse, J.W., Haas, R.H., Schell, J.A., Deering, D.W., 1974. Monitoring vegetation systems in the Great Plains with ERTS. In: Proceedings of the Third ERTS Symposium, NASA, SP-351, 1. NASA, Washington, DC, pp. 309–317.

Ruiz, J., Polo, M.J., Díez-Minguito, M., Navarro, G., Morris, E.P., Huertas, I.E., Caballero, I., Contreras, E., Losada, M.A. (2015) The Guadalquivir estuary: a hot spot for environmental and human conflicts. *In: C.W. Finkl and C. Majowski (eds.), Environmental Management and Governance Coastal Research Library, Chapter 8, Vol. 8*, pp: 199–232. DOI:https://doi.org/10.1007/978-3-319-06305-8_8.

Savelli, R., Serôdio, J., Cugier, P., Méléder, V., Polsenaere, P., Dupuy, C., Le Fouest, V., 2021. Potential impact of photoinhibition on microphytobenthic primary production on a large intertidal mudflat. J. Geophys. Res. Biogeosci. 126 (9), e2021JG006443. https://doi.org/10.1029/2021JG006443.

Spilmont, N., Davoult, D., Migné, A., 2006. Benthic primary production during emersion: in-situ measurements and potential primary production in the Seine Estuary (English Channel, France). Mar. Pollut. Bull. 53, 49–55. https://doi.org/10.1016/j.marpolbul.2005.09.016.

Stal, L.J., 2010. Microphytobenthos as a biogeomorphological force in intertidal sediment stabilization. Ecol. Eng. 36 (2), 236–245. https://doi.org/10.1016/j.ecoleng.2008.12.032.

Trobajo, R., Sullivan, M.J., 2010. Applied diatom studies in estuaries and shallow coastal environments. In: Smol, J.P., Stoermer, E.F. (Eds.), The Diatoms: Applications for the Environmental and Earth Sciences. Cambridge University Press, pp. 309–323. https://doi.org/10.1017/CBO9780511763175.017.

Tucker, C.J., 1979. Red and photographic infrared linear combinations for monitoring vegetation. Remote Sens. Environ. 8 (2), 127–150. https://doi.org/10.1016/0034-4257(79)90013-0.

Underwood, G.J.C., Kromkamp, J., 1999. Primary production by phytoplankton and microphytobenthos in estuaries. Adv. Ecol. Res. 29, 93–153. https://doi.org/10.1016/S0065-2504(08)60192-0.

Underwood, G.J.C., Philips, J., Saunders, K., 1998. Distribution of estuarine benthic diatom species along salinity and nutrient gradients. Eur. J. Philos. 35, 116–125. https://doi.org/10.1080/09670269810001736673.

Underwood, G.J.C., Dumbrell, A.J., McGenity, T.J., McKew B. A., Whitby C. (2022) The Microbiome of Coastal Sediments. Chapter 12, In the Marine Microbiome (Eds: Lucas J. Stal & Silvia Cretoiu), Springer Nature Switzerland AG. ISBN: 978-3-030-90382-4.

UNESCO MAB (n.d.) Man and the Biosphere Programme. Available online: https://www.unesco.org/en/mab/donana (accessed 04-07-2024).

UNESCO WHC (n.d.) World Heritage List. Available online: http://whc.unesco.org/en/list/685/ (accessed 04-07-2024).

Van der Wal, D., Wielemaker-Van den Dool, A., Herman, P.M.J., 2010. Spatial synchrony in intertidal benthic algal biomass in temperate coastal and estuarine ecosystems. Ecosystems 13, 338–531. https://doi.org/10.1007/s10021-010-9322-9.

Wang, X., Xiao, X., Zou, Z., Chen, B., Ma, J., Dong, J., Doughty, R.B., Zhong, Q., Qin, Y., Dai, S., Li, X., Zhao, B., Li, B., 2018. Tracking annual changes of coastal tidal flats in China during 1986–2016 through analyses of Landsat images with Google Earth Engine. Remote Sens. Environ. 238, 110987. https://doi.org/10.1016/j.rse.2018.11.030.

Zhang, T., Tian, B., Wang, Y., Liu, D., Sun, S., Duan, Y., Zhou, Y., 2021. Quantifying seasonal variations in microphytobenthos biomass on estuarine tidal flats using Sentinel-1/2 data. Sci. Total Environ. 777, 146051. https://doi.org/10.1016/j.scitotenv.2021.146051.